Supporting Information

for

Origin of Long Lifetime of Band-Edge Charge Carriers in Organic-Inorganic Lead Iodide Perovskites

Tianran Chen, Wei-Liang Chen, Benjamin J. Foley, Jooseop Lee, Jacob Ruff, J. Y. Peter Ko, Craig M. Brown, Leland W. Harriger, Depei Zhang, Changwon Park, Mina Yoon, Yu-Ming Chang, Joshua J. Choi, and Seung-Hun Lee

This PDF file includes:

Sample preparation

PbI_2 (99.999%) in a powder form and gamma-butyrolactone (gBL) (99%) in a liquid form were purchased from Sigma-Aldrich. Formamidinium iodide ($HC(NH_2)_2I$) and methylammonium iodide (MAI) in a powder form were purchased from Dyesol.

3.58 grams of $HC(NH_2)_2PbI_3$ and 9.38 grams of PbI_2 were added to 30 mL of gBL. The solution was dissolved at 150 ^oC, and heated at the same temperature in ambient conditions for approximately 8 hours in an evaporating dish until the solvent had evaporated and black crystals were visible. The sample was then cooled to room temperature, and the yellow solid was collected and further dried in a nitrogen glovebox for 2 hours at 100 ^oC. 12.47 grams of yellow powder were collected. This powder turned back upon heating to 170 ^oC, and returned to its original color upon cooling. $CH_3NH_3PbI_3$ was synthesized using the same method as reported before (S1).

Experimental procedure of the photoluminescence measurements

The temperature dependent photoluminescence (PL) measurements were performed on a custom-built laser scanning confocal system coupled to a temperature controlled vacuum stage (Linkam THMS350V). The excitation from a 450 nm pico-second pulsed laser with a repetition rate of 1 MHz, was focus with a 5× objective (Olympus, MPLanFL N, NA 0.15) onto the sample. The on-sample power was ~0.4 μW. The PL spectra were acquired using a custom-built spectrometer with a thermoelectric-cooled CCD (Andor iDus). Spectra were obtained 2 minutes after reaching each set temperature. For better statistics, we used the average spectrum from a 5×5 spectral mapping covering an area of 56×56 μm^2. The integration time for each spectrum was 4 s.

Fig. S1 shows the Full-Width-at-Half-Maximum (FWHM) of the main emission peaks of the PL data (see Fig. 1) taken from a powder sample of $HC(NH_2)_2PbI_3$ for HEAT1 (blue circles) and HEAT2 (red squares). For HEAT2, there exist two emission peaks around 1.46 eV for $140\ \mathrm{K} \leq T \leq 220\ \mathrm{K}$. The FWHMs of the two peaks are similar and in Fig. S1 only the FWHM of the stronger peak is shown.

Fig. S2 shows the Full-Width-at-Half-Maximum (FWHM) of the main emission peaks of the PL data (see Fig. 2) taken from a powder sample of $NH_3CH_3PbI_3$. The FHWMs are similarly narrow

as those of the tetragonal and cubic phases of $HC(NH_2)_2PbI_3$. These indicate that the tetragonal and cubic phases of both HOIPs have direct bandgap.

Experimental procedure and analysis of the time-resolved photoluminescence

For the time-resolved photoluminescence (TRPL) measurements, the PL signal from the sample was sent into a custom-built monochromator coupled with a photomultiplier tube (PMT) detector, allowing for TRPL measurement of the desired wavelength of the PL spectrum. The monochromator contains an adjustable detection slit that was set for a 15 nm bandwidth detection. Finally, the PMT signal was sent to the time correlated single photon counting (TCSPC) device (PicoQuant, PicoHarp 300) for TRPL measurements.

To determine the PL lifetime, we used the commercial software FluoFit (PicoQuant), and fitted the TRPL data to a two-exponential re-convolution function

$$I(t) = \int_{-\infty}^{t} IRF(t') \left[A_1 e^{-\frac{t-t'}{\tau_1}} + A_2 e^{-\frac{t-t'}{\tau_2}} \right] \mathrm{d}t' \qquad (1)$$

Here t is the delay time between the laser pulse and PL emission, *IRF* is the instrument response function, and A_1, A_2 and τ_1, τ_2 are the amplitude and lifetime of the exponential components respectively. The thick smooth lines in Fig. 5 and 6 are the fitting results and the fitted parameters are listed in Tables S1, S2, and S3. In our system, the *IRF* has a FWHM of 0.3 ns. When the lifetime approaches that of the *IRF*, the TRPL curve would show features of the *IRF*. The phenomenological fitting employed here does not distinguish the first, second and third order kinetics that have been assigned to trap-mediated recombination, radiative biomolecular recombination and Auger recombination respectively (S2). Distinguishing them requires a detailed TRPL study with various excitation light fluence at each temperature, which is beyond the scope of this work. Instead, our approach here was to study the temperature dependence of TRPL with the same sample in which the defect density is expected to increase monotonically with temperature. Thus, the observed discontinuous anomalous lifetime behaviors as a function of temperature cannot be explained in terms of defect density. In particular, the jump in lifetime by up to two orders of magnitude when the system enters the high organic cation rotation entropy phase warrants that our analysis is sufficient for the purpose of this work. Nonetheless, further

studies on detailed TRPL measurements and analysis as a function of excitation light intensity and temperature will be valuable.

Neutron scattering methods and data

NIST NCNR SPINS: The elastic neutron scattering data were obtained at the cold neutron triple-axis spectrometer, SPINS at the NIST Center for Neutron Research (NCNR) located in Gaithersburg, Maryland. Each of non-deuterated $HC(NH_2)_2PbI_3$ (~10 g) and $CH_3NH_3PbI_3$ (~10 g) sample was placed into a cylindrical aluminum can in a dry helium box. The aluminum can was sealed with a lead o-ring. The sample can was mounted in a closed cycle helium 2rigerator and the temperature was changed in the range of 8.2 K – 450 K. The energy of the neutrons was 5 meV. The collimations were open - 80'- 80'- open, from the cold neutron guide to the monochromator to the sample to the analyzer to the detector. The higher order neutron contaminations were eliminated by placing two liquid nitrogen cooled beryllium filters before and after the sample.

Note that similar data obtained from deuterated $HC(ND_2)_2PbI_3$ have been reported in Ref. (S3). The hexagonal-to-cubic phase transition temperature for non-deuterated $HC(NH_2)_2PbI_3$, $T_{cubic}^{HEAT1} = 400(20)$ K (see Fig. 3*A* and 3*B*), is higher than that for $HC(ND_2)_2PbI_3$ that is 350(5) K. The difference in T_{cubic}^{HEAT1} is due to the fact that the transition is driven by the entropy caused by the isotropic rotations of the FA^+ cation, $S_{rot} = \frac{3}{2}k_B\{1 + \ln(0.4786\, k_B T\, \sqrt[3]{I_1 I_2 I_3})\}$ where k_B is the Boltzmann constant; $HC(NH_2)_2PbI_3$ has smaller principle moment of inertia $(I_i \approx 8.586, 48.851, 57.436\ \text{u}\text{Å}^2)$ than $HC(ND_2)_2PbI_3$ does $(I_i \approx 11.644, 60.161, 71.806\ \text{u}\text{Å}^2)$ where the unified atomic mass unit, u, is $1.6605e^{-27}$ kg. Thus, their temperature difference in the entropy-driven transition is estimated to be $\Delta T_c = 55$ K, which is consistent with our experimental observation.

Fig. S3 shows the elastic neutron scattering data obtained from $NH_3CH_3PbI_3$ as a function of temperature. $NH_3CH_3PbI_3$ undergoes an orthorhombic-to-tetragonal phase transition at 164(2) K, and a tetragonal-to-cubic phase transition at 325(3) K.

NIST NCNR BT1: To determine the crystal structures of the quenched phases, neutron powder diffraction (NPD) measurements were performed, using the BT1 diffractometer at NCNR. The

wavelength of incident neutrons, λ = 1.5398 Å, was selected using a Cu (311) monochromator with an in-pile 60' collimator. The scattered neutrons were collected by 32 3-He detectors over the 2θ range of 1.3°– 166.3° with 0.05° step size. A 10 g sample of $HC(ND_2)_2PbI_3$ was placed into a cylindrical vanadium can in a dry helium box. The vanadium can was sealed with an indium o-ring. The sample can was mounted in a closed cycle helium refrigerator.

Fig. S4 shows the neutron diffraction pattern obtained at 100 K (Tet LT) and 200 K (Tet IT) in the HEAT1 process. The main difference between 100 K and 200 K is that at 100 K there exists a set of superlattice peaks that can be indexed with a characteristic wave vector of $q = \left(0,0,\frac{1}{6}\right)$. The data were refined simultaneously with synchrotron x-ray data shown in Fig. S4 to determine the quenched structures to be tetragonal; the $P4/mbm$ tetragonal (Tet LT) for $T < T_{Tet\ LT}^{HEAT2} = 140(10)$ K and the $P4bm$ tetragonal (Tet IT) for $T_{Tet\ LT}^{HEAT2} < T < T_{Cubic}^{HEAT2}$. The crystal structures of the Tet IT and Tet LT phases were determined by simultaneous refinement of the neutron diffraction data and the x-ray data shown as solid lines in Fig. S4 and S5. Their structural parameters are listed in Table S3 (Tet IT) and S4 (Tet LT). Here we emphasize that the neutron powder diffraction refinement result shows that $HC(NH_2)_2^+$ cations in Tet IT phase have strongly preferential orientations (see Fig. 4*C*). On the contrary, $HC(NH_2)_2^+$ cations have isotropic orientations in the cubic phase (see Fig. 4*A*) (S3).

Synchrotron x-ray scattering methods and data

Synchrotron x-ray powder diffraction has been measured at the F2 beam line at the Cornell High Energy Synchrotron Source (CHESS). Diffraction patterns with the Q range from 0.3 $Å^{-1}$ to 9.3 $Å^{-1}$ were collected with incident wavelength 0.202153 Å and a 2D flat panel detector. The powder was sealed inside a 1 mm diameter Kapton capillary, and was rotated 360° during data collection to achieve ideal powder averaging.

The sample of $HC(NH_2)_2PbI_3$ was heated *ex situ* for 30 minutes at 450K, where the color fully turned black. It then was cooled down to 100 K at the rate of 4 K/min using a liquid nitrogen cryostream. The data were collected while warming the sample from 100 K to 300 K with 25 K steps. Each measurement involved 12 rotations amounting to 2.5 hours beam exposure for every temperature step.

Table S3 and S4 in the Supporting Information list the structural parameters for the Tet LT and Tet IT phases of $HC(NH_2)_2PbI_3$.

Fig. S5 shows the synchrotron X-ray powder diffraction data at three different temperatures, 300 K (cubic phase), 200 K (Tet IT phase) and 100 K (Tet LT phase). As shown in the lower panel, the Tet LT phase exhibit a set of weak supperlattice peaks characterized with $q = \left(0,0,\frac{1}{6}\right)$. This means that the Tet LT phase adopts a 1×1×6 supercell, compared to the Tet IT phase.

Fig. S6 summarizes the temperature dependence of the lattice constants of $FAPbI_3$: the lattice constants determined with neutron diffraction data (squares) and with synchrotron x-ray data (triangles).

Density Functional Theory Calculations

Our first principles density functional theory calculations (DFT) use projector augmented wave (S4) to describe the core electrons and the generalized gradient approximation with the Perdew-Burke-Ernzerhof functional (S5), as implemented in VASP (Vienna *Ab initio* Simulation Package) code (S6). 4×4×4 k-points are sampled through Monkhorst-Pack scheme (S7) for cubic unit cell and equivalent and denser sampling was used for tetragonal and hexagonal unit cells.
The lattice constants and atomic coordinates are obtained from Rietveld refinement of X-ray and neutron diffraction experiments. Lead (Pb) and Iodine (I) atoms are fixed and $HC(NH_2)_2^+$ cations are fully relaxed until the force on each atom is less than 0.02 eV/Å. However, since the optimization is performed at zero temperature, $HC(NH_2)_2^+$ cations remain frozen at the local minimum near the assigned orientation. Such a frozen $HC(NH_2)_2^+$ cation can locally break the cubic/tetragonal/hexagonal symmetry, thus the calculated formation entropy and electronic band structures have some ambiguity in our calculation settings. After the fully relaxation of $HC(NH_2)_2^+$ cations is reached, non-self-consistent field calculation is performed and electronic band structures are calculated on selected k-point-paths (Γ-X-M-Γ-R-X for cubic structure, Γ-K-H-A-Γ-M-L-A for hexagonal structure, and Γ-X-M- Γ-Z-R-A for tetragonal structure).

Fig. S7 shows the electronic band structure of $HC(NH_2)_2PbI_3$ for the cubic, Hex IT and Tet IT phases. We note that for the cubic phase we assumed a ferro-oriented pattern of the FA^+ actions in which the planar FA^+ cations lie in the central mirror plane of the unit cell and the C–H bond

is directed into a cube face. The orientations of each FA^+ cation in different unit cells were assumed to be the same. This was necessary for the limitation of DFT calculations being done at zero temperature. For other phases the DFT calculations were performed on the experimentally determined structures. Fig. S8 shows the electronic band structures for the Hex LT and Tet LT phases that were obtained by DFT calculations. The crystal structures for Hex IT phases were taken from Ref. (S3), while the crystal structure of the Tet LT phase was determined by Rietveld refinement of neutron diffraction and synchrotron x-ray data taken at 100 K. Tet LT phase has sharp cone-shape bands with direct bandgap, similar to Tet IT phase. In contrast, the Hex LT phase has nearly flat valence and conduction bands with indirect bandgap, similar to Hex IT phase. This is consistent with the PL data shown in the main text.

Fig. S9 shows the calculated electronic band structures for the cubic, tetragonal, and orthorhombic phases of $CH_3NH_3PbI_3$. All phases show similar direct band gaps, which is consistent with their PL data shown in Fig. 2 and S2.

The electronic charge densities of $CH_3NH_3^+$ and $HC(NH_2)_2^+$ cations were calculated using VASP package. Pb and I atoms were not involved in the calculation. Instead, a constant charge density background was added to neutralize the cation. In order to show clearly the electric polarity in the molecule, the calculated charge density was then subtracted from a direct sum of single-atom charge densities of each atom (which have negligible dipole and quadrupole moment). The subtracted "excessive" charge density is plotted in Fig. S10. The blue and red surfaces are isosurfaces of "excessive" electrons and holes, respectively.

Analysis of thermal factors

Isotropic thermal factors of Pb, I and organic cation of $FAPbI_3$ (Fig. S11) and $MAPbI_3$ (Fig. S12) as a function of temperature were obtained through Rietveld refinement of synchrotron X-ray and neutron diffraction data. As shown in Fig. S11 and S12, the thermal factors of inorganic atoms and organic molecules do not show any abrupt anomalies at the phase transition temperatures where we observe sudden jumps in PL lifetime. This suggests that the contributions from the local fluctuations of inorganic atoms and phonons are not responsible for the abrupt jump observed in PL lifetime.

References

S1. Zhu H, *et al*. (2016) Screening in crystalline liquids protects energetic carriers in hybrid perovskites. *Science* 353(6306):1409-1413.

S2. Stranks SD, *et al*. (2014) Recombination Kinetics in Organic-Inorganic Perovskites: Excitons, Free Charge, and Subgap States. *Phys. Rev. Applied* 2(3):034007.

S3. Chen T, *et al*. (2016) Entropy-driven structural transition and kinetic trapping in formamidinium lead iodide perovskite. *Science Advances* 2(10):e1601650.

S4. Kresse G & Joubert D (1999) From ultrasoft pseudopotentials to the projector augmented-wave method. *Phys. Rev. B* 59(3):1758-1775.

S5. Perdew JP, Burke K, & Ernzerhof M (1996) Generalized Gradient Approximation Made Simple. *Phys. Rev. Lett*. 77(18):3865-3868.

S6. Kresse G & Furthmüller J (1996) Efficiency of ab-initio total energy calculations for metals and semiconductors using a plane-wave basis set. *Computational Materials Science* 6(1):15-50.

S7. Monkhorst HJ & Pack JD (1976) Special points for Brillouin-zone integrations. *Phys. Rev. B* 13(12):5188-5192.

S8. Chen T, *et al*. (2015) Rotational dynamics of organic cations in the $CH_3NH_3PbI_3$ perovskite. *Phys. Chem. Chem. Phys*. 17(46):31278-31286.

S9. Weller MT, Weber OJ, Henry PF, Pumpo AMD, & Hansen TC (2015) Complete structure and cation orientation in the perovskite photovoltaic methylammonium lead iodide between 100 and 352 K. *Chem. Commun*. 51(20):4180-4183.

Tables

Table S1. $HC(NH_2)_2PbI_3$: Fitted parameters for TRPL of HEAT1. Results of reconvolution fit for the TRPL of HEAT1 measurements. For 420K and 440K, the TRPL integration time was 3 minutes. For all other temperatures, the integration time was 1 minute.

Temperature (K)	Detection Wavelength (nm)	A_1	τ_1 (ns)	A_2	τ_2 (ns)	Background
80	680	120(4)	790(20)	110(100)	4(4)	16(1)
120	660	110(10)	110(10)	90(30)	30(10)	7.3(5)
140	660	250(40)	22(2)	880(120)	6.2(8)	7.7(5)
160	700	90(30)	11(4)	350(150)	1.6(7)	7.9(5)
200	680	25(26)	11(12)	600(200)	1.1(4)	9.0(5)
240	670	60(40)	8(4)	3000(700)	0.45(9)	10.6(6)
280	660	150(110)	1.7(1)	4300(1500)	0.15(5)	8.1(5)
320	650	120(140)	1.1(10)	5600(2400)	0.08(3)	7.8(5)
360	640	73(130)	1(1)	7000(4300)	0.04(2)	7.5(5)
420	780	12(9)	120(120)	10(30)	15(40)	24.4(8)
440	790	16(5)	300(100)	30(40)	8(13)	22.7(8)

Table S2. $HC(NH_2)_2PbI_3$: Fitted parameters for TRPL of HEAT2. Results of reconvolution fit for the TRPL of HEAT2 measurements. For 420K, the TRPL integration time was 3 minutes. For all other temperatures, the integration time was 1 minute.

Temperature (K)	Detection Wavelength (nm)	A_1	τ_1 (ns)	A_2	τ_2 (ns)	Background
80	850	120(20)	39(6)	550(110)	4.4(9)	7.2(5)
120	830	150(25)	29(4)	1400(200)	3.4(4)	7.2(5)
160	840	22(15)	22(17)	120(70)	2.3(6)	6.7(5)
240	820	56(26)	11(5)	270(140)	1.4(7)	6.6(4)
260	820	96(19)	32(6)	590(130)	3.1(7)	6.9(5)
280	830	119(6)	310(15)	200(60)	9(3)	13.0(8)
320	820	34(5)	210(40)	170(50)	7(2)	8.9(6)
360	830	19(4)	230(60)	80(40)	6(4)	8.0(5)
400	800	20(4)	290(77)	70(40)	6(4)	7.6(5)
420	800	17(6)	260(110)	50(50)	6(7)	23.8(8)

Table S3. $CH_3NH_3PbI_3$: Fitted parameters for TRPL. Results of reconvolution fit for the TRPL data of $CH_3NH_3PbI_3$. The TRPL integration time was 3 minutes.

Temperature (K)	Detection Wavelength (nm)	A_1	τ_1 (ns)	A_2	τ_2 (ns)	Background
80	785	260(20)	60(3)	1600(100)	5.7(4)	8.6(8)
100	775	360(20)	40(2)	2600(200)	4.1(3)	8.3(7)
120	775	1200(80)	14.6(6)	12200(600)	1.88(9)	7.2(7)
140	775	1380(70)	12.1(4)	9700(500)	1.68(8)	7.6(9)
160	790	1560(80)	5.9(2)	3100(300)	1.4(1)	6.7(6)
180	785	160(20)	24(2)	2800(200)	1.8(1)	6.4(7)
200	780	180(20)	16(1)	1500(100)	2.3(2)	6.5(6)
240	770	1150(60)	9.0(3)	5300(300)	1.51(9)	6.6(6)
280	770	320(40)	5.7(5)	3600(300)	0.72(6)	6.0(5)
300	770	770(50)	6.4(3)	2800(200)	1.5(1)	5.9(5)
320	770	570(50)	7.1(4)	3200(200)	1.5(1)	5.8(5)
340	770	90(20)	10(2)	730(90)	1.5(1)	5.5(4)
360	770	190(20)	10.3(9)	1400(100)	1.5(1)	5.7(5)
370	760	40(10)	12(3)	640(80)	1.5(1)	5.5(4)
380	770	30(10)	12(4)	270(60)	1.5(1)	5.5(4)

Table S4. $HC(NH_2)_2PbI_3$: Refined structural parameters of $HC(NH_2)_2PbI_3$ Tet IT phase for 200 K. Positions within tetragonal $P4/mbm$ and occupancies per chemical unit cell (c.u.) in $FAPbI_3$ at $T = 200$ K were determined using Rietveld analysis of neutron diffraction data shown in Fig. 1 and 2. The lattice parameters are a = 8.9258(3) Å, c = 6.3259(4) Å. $\chi^2 = 0.8673$.

Atom	Wyck	x	y	z	Occ	U_{iso}(Å^2)
Pb	2a	0	0	0	1	0.019(1)
I1	2b	0	0	0.5	1	0.040(1)
I2	4g	0.7165(5)	0.7835(5)	0	1	=I1 U_{iso}
N1	16l	0.4368(88)	0.8967 (68)	0.4524(104)	1/8	0.088(3)
N2	16l	0.5752(83)	0.1161(72)	0.4612(120)	1/8	=N1 U_{iso}
C	16l	0.5293(32)	0.9900(41)	0.5429(29)	1/8	=N1 U_{iso}
H	16l	0.5715(168)	0.9600(150)	0.6998(162)	1/8	=N1 U_{iso}
D1	16l	0.3897(66)	0.9123(64)	0.3059(68)	1/8	=N1 U_{iso}
D2	16l	0.6476(58)	0.1802(78)	0.5463(79)	1/8	=N1 U_{iso}
D3	16l	0.4087(50)	0.8014(58)	0.5312(123)	1/8	=N1 U_{iso}
D4	16l	0.5437(46)	0.1564(52)	0.3156(89)	1/8	=N1 U_{iso}

Table S5. $HC(NH_2)_2PbI_3$: Refined structural parameters of $HC(NH_2)_2PbI_3$ Tet LT phase for 100 K. Positions within hexagonal $P4bm$ and occupancies per chemical unit cell (c.u.) in $FAPbI_3$ at $T = 100$ K were determined using Rietveld analysis of the neutron diffraction data shown in Fig. 1*C*. The lattice parameters are a = 8.8774(1) Å, c = 37.6724(14) Å. $\chi^2 = 1.270$.

Atom	Wyck	x	y	Z	Occ	U_{iso}(Å^2)
Pb1	2a	0	0	0.0016(7)	1	0.007(1)
Pb2	2a	0	0	0.5034(6)	1	=Pb1 U_{iso}
Pb3	2a	0	0	0.8320(5)	1	=Pb1 U_{iso}
Pb4	2a	0	0	0.3384(5)	1	=Pb1 U_{iso}
Pb5	2a	0	0	0.1672(6)	1	=Pb1 U_{iso}
Pb6	2a	0	0	0.6698(6)	1	=Pb1 U_{iso}
I1	2a	0	0	0.4180(15)	1	0.030(1)
I2	2a	0	0	0.9170(15)	1	=I1 U_{iso}
I3	4c	0.7857(24)	0.2857(24)	0.1618(11)	1	=I1 U_{iso}
I4	4c	0.7927(22)	0.2927(22)	0.6683(13)	1	=I1 U_{iso}
I5	2a	0	0	-0.7475(15)	1	=I1 U_{iso}
I6	2a	0	0	0.7543(14)	1	=I1 U_{iso}
I7	2a	0	0	0.5860(17)	1	=I1 U_{iso}
I8	2a	0	0	0.0881(16)	1	=I1 U_{iso}
I9	4c	0.8032(25)	0.3032(25)	-0.0004(14)	1	=I1 U_{iso}
I10	4c	0.7473(33)	0.2473(33)	0.4893(7)	1	=I1 U_{iso}
I11	4c	0.7840(22)	0.2840(22)	0.8294(11)	1	=I1 U_{iso}
I12	4c	0.7824(26)	0.2824(26)	0.3245(10)	1	=I1 U_{iso}
N1	8d	0.6061(133)	0.0805(162)	0.0846(124)	1/4	0.023(1)
N2	8d	0.4218(161)	-0.1040(137)	0.0860(124)	1/4	=N1 U_{iso}
N3	8d	0.5423(26)	-0.0016(60)	0.5812(5)	1/4	=N1 U_{iso}
N4	8d	0.4696(27)	-0.0138(61)	0.6402(5)	1/4	=N1 U_{iso}
N5	8d	0.6104(35)	-0.0557(39)	0.4092(8)	1/4	=N1 U_{iso}
N6	8d	0.3574(34)	-0.0348(38)	0.4234(8)	1/4	=N1 U_{iso}
N7	8d	0.5953(57)	0.0872(53)	0.9209(8)	1/4	=N1 U_{iso}
N8	8d	0.4201(57)	-0.1048(54)	0.9263(8)	1/4	=N1 U_{iso}
N9	8d	0.5849(39)	0.0838(41)	0.2547(10)	1/4	=N1 U_{iso}
N10	8d	0.3655(37)	-0.0400(38)	0.2387(11)	1/4	=N1 U_{iso}
N11	8d	0.5799(51)	0.0986(51)	0.7631(7)	1/4	=N1 U_{iso}
N12	8d	0.4074(51)	-0.0937(50)	0.7545(8)	1/4	=N1 U_{iso}
C1	8d	0.4672(59)	0.0354(56)	0.0885(8)	1/4	=N1 U_{iso}
C2	8d	0.4427(18)	-0.0225(35)	0.6062(5)	1/4	=N1 U_{iso}
C3	8d	0.4985(35)	0.0038(29)	0.4268(6)	1/4	=N1 U_{iso}
C4	8d	0.4972(40)	-0.0071(38)	0.9078(4)	1/4	=N1 U_{iso}
C5	8d	0.4967(37)	0.0188(34)	0.2316(6)	1/4	=N1 U_{iso}
C6	8d	0.4999(42)	0.0096(43)	0.7430(4)	1/4	=N1 U_{iso}
H1	8d	0.3821(182)	0.1212(167)	0.0942(20)	1/4	=N1 U_{iso}

H2	8d	0.3275(21)	-0.0495(42)	0.5980(8)	1/4	=N1 U_{iso}
H3	8d	0.5250(50)	0.0932(49)	0.4458(12)	1/4	=N1 U_{iso}
H4	8d	0.4780(53)	-0.0039(56)	0.8791(5)	1/4	=N1 U_{iso}
H5	8d	0.5358(55)	0.0132(64)	0.2041(7)	1/4	=N1 U_{iso}
H6	8d	0.5112(54)	0.0225(54)	0.7142(4)	1/4	=N1 U_{iso}
D1	8d	0.6957(87)	0.0110(277)	0.0792(138)	1/4	=N1 U_{iso}
D2	8d	0.3104(210)	-0.1262(295)	0.0896(214)	1/4	=N1 U_{iso}
D3	8d	0.6285(294)	0.1924(218)	0.0871(214)	1/4	=N1 U_{iso}
D4	8d	0.4907(285)	-0.1943(91)	0.0808(139)	1/4	=N1 U_{iso}
D5	8d	0.6536(23)	0.0242(61)	0.5855(8)	1/4	=N1 U_{iso}
D6	8d	0.3831(35)	-0.0323(90)	0.6573(6)	1/4	=N1 U_{iso}
D7	8d	0.5084(40)	-0.0113(95)	0.5555(5)	1/4	=N1 U_{iso}
D8	8d	0.5728(35)	0.0106(73)	0.6511(6)	1/4	=N1 U_{iso}
D9	8d	0.5999(48)	-0.1402(55)	0.3907(12)	1/4	=N1 U_{iso}
D10	8d	0.2794(40)	0.0195(59)	0.4385(12)	1/4	=N1 U_{iso}
D11	8d	0.7161(34)	-0.0166(54)	0.4140(12)	1/4	=N1 U_{iso}
D12	8d	0.3184(40)	-0.1169(46)	0.4065(11)	1/4	=N1 U_{iso}
D13	8d	0.6230(65)	0.0951(64)	0.9473(10)	1/4	=N1 U_{iso}
D14	8d	0.3465(82)	-0.1729(77)	0.9132(13)	1/4	=N1 U_{iso}
D15	8d	0.6489(84)	0.1586(79)	0.9040(13)	1/4	=N1 U_{iso}
D16	8d	0.4282(67)	-0.1186(66)	0.9533(9)	1/4	=N1 U_{iso}
D17	8d	0.5608(56)	0.0959(68)	0.2812(10)	1/4	=N1 U_{iso}
D18	8d	0.3062(49)	-0.0879(62)	0.2186(15)	1/4	=N1 U_{iso}
D19	8d	0.6850(41)	0.1258(51)	0.2461(16)	1/4	=N1 U_{iso}
D20	8d	0.3167(43)	-0.0418(49)	0.2635(13)	1/4	=N1 U_{iso}
D21	8d	0.5791(60)	0.0974(60)	0.7904(7)	1/4	=N1 U_{iso}
D22	8d	0.3507(68)	-0.1568(65)	0.7364(11)	1/4	=N1 U_{iso}
D23	8d	0.6485(67)	0.1752(63)	0.7512(12)	1/4	=N1 U_{iso}
D24	8d	0.3872(59)	-0.1166(56)	0.7808(9)	1/4	=N1 U_{iso}

Fig. S1

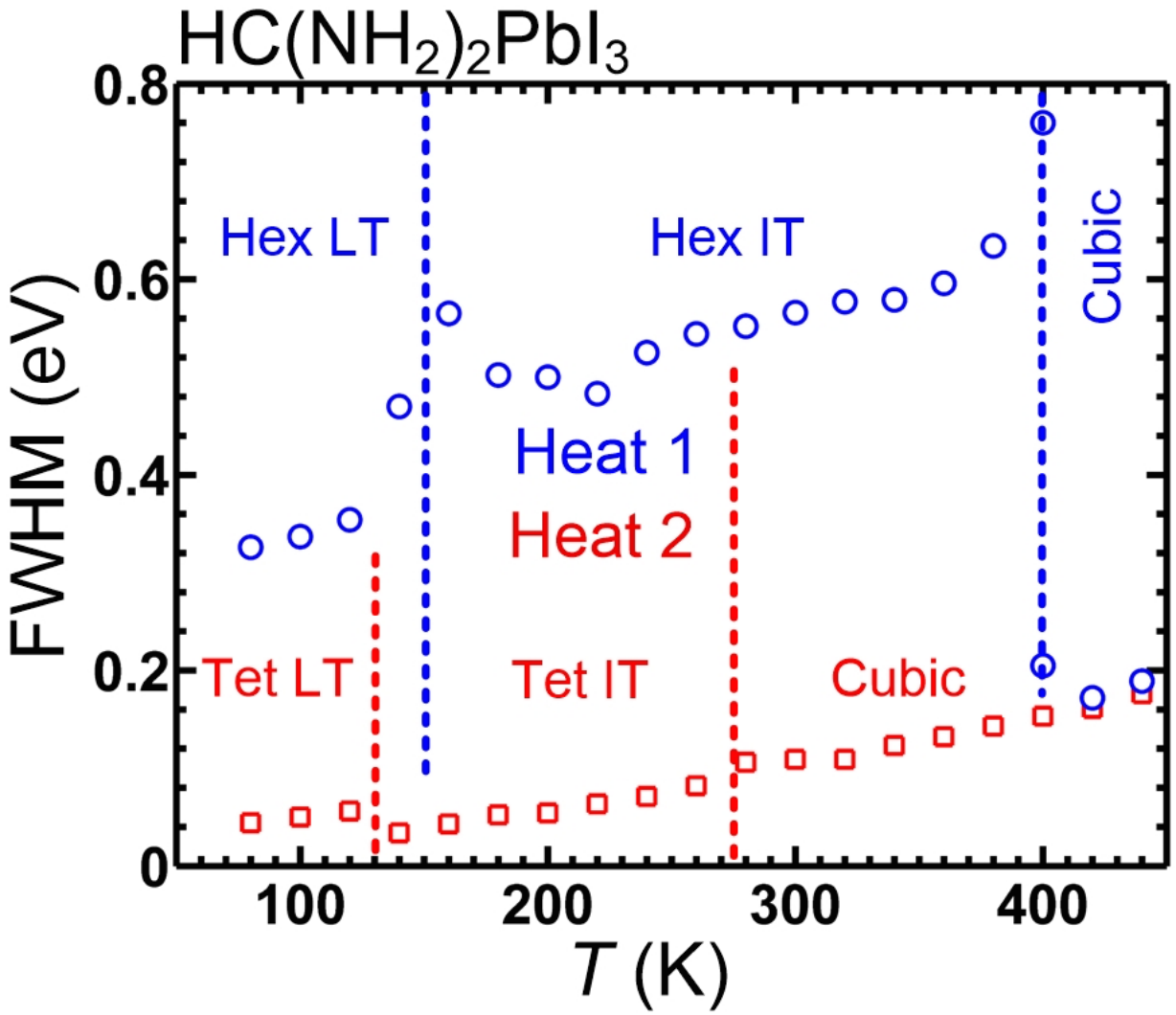

Fig. S1: Full-width-at-half-maximum (FWHM) of emission peaks of PL spectra of $HC(NH_2)_2PbI_3$. Blue circles and the red squares are the FWHMs of the main emission peaks of the PL data of $HC(NH_2)_2PbI_3$ shown in Fig. 1 for HEAT1 and HEAT2, respectively. For HEAT2, there exist two emission peaks for $140\ \text{K} \leq T \leq 220\ \text{K}$, and their FWHMs are similar and the FWHMs of the stronger peak are shown here.

Fig. S2

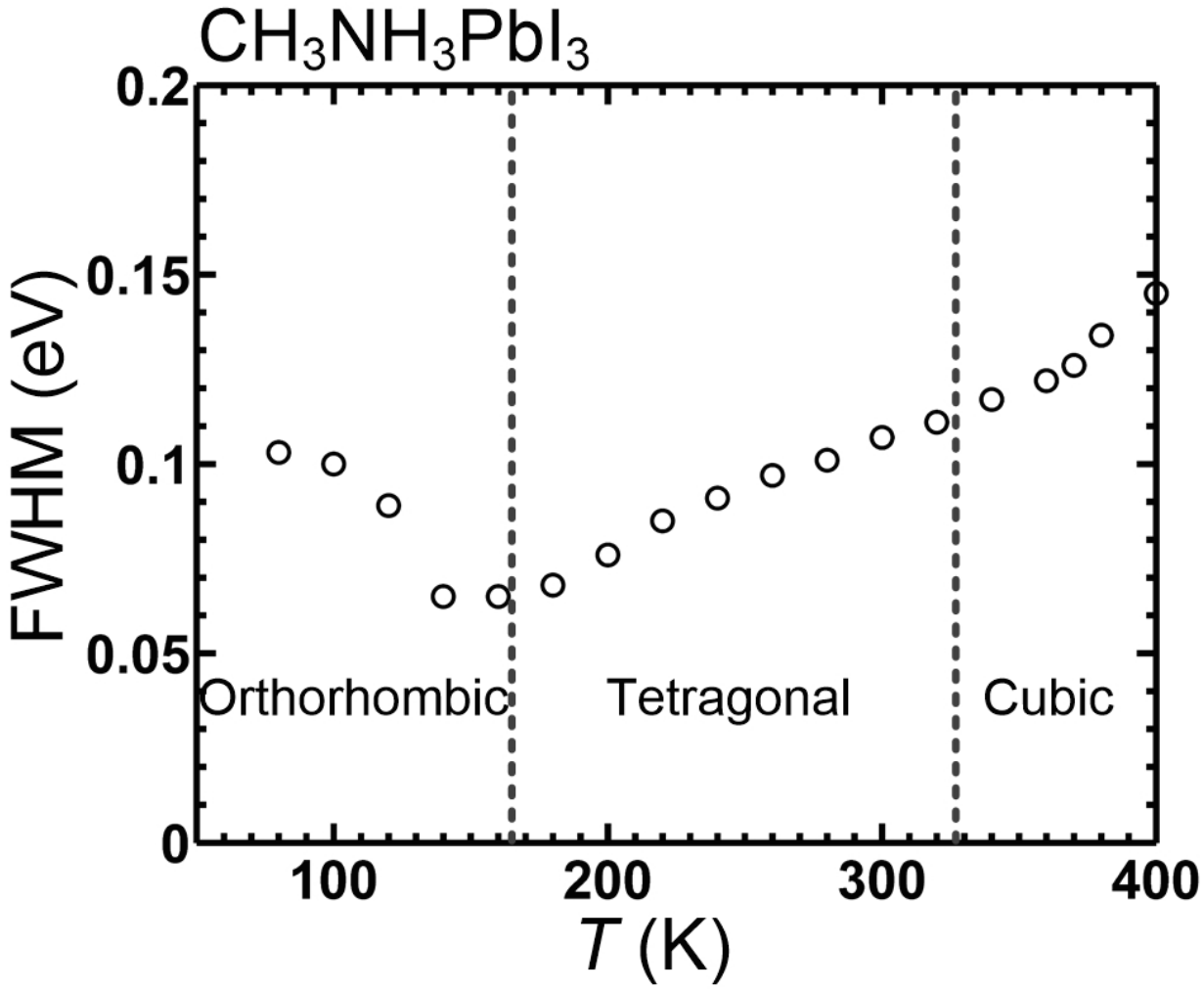

Fig. S2: Full-width-at-half-maximum (FWHM) of emission peaks of PL spectra of $CH_3NH_3PbI_3$. Blue circles and the red squares are the FWHMs of the main emission peaks of the PL data of $CH_3NH_3PbI_3$ shown in Fig. 2.

Fig. S3

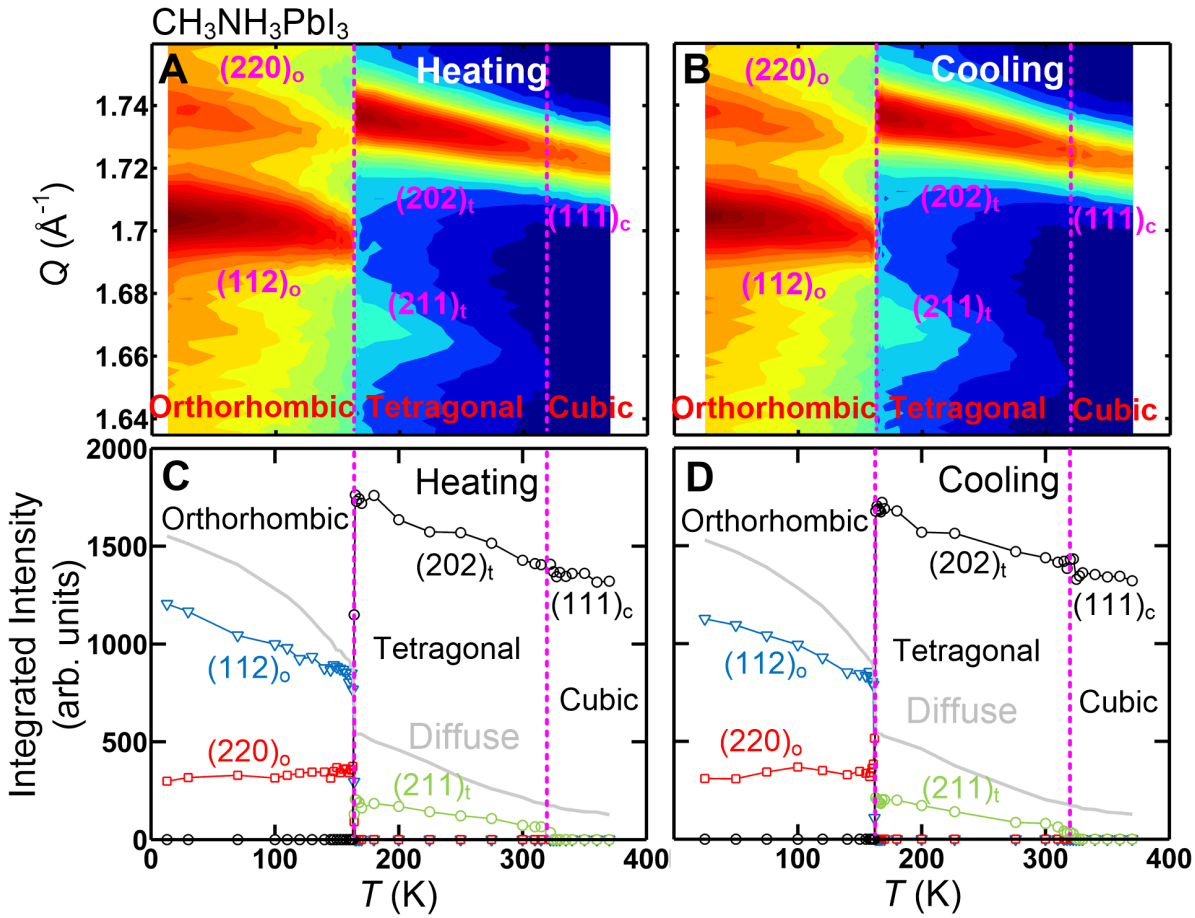

Fig. S3. Structural transitions of $CH_3NH_3PbI_3$. Elastic neutron scattering data were obtained at SPINS, NCNR. (*A*) and (*B*) shows a contour map of the scattering intensity as a function of momentum transfer, *Q*, and temperature, *T*. (*C*) and (*D*) shows the integrated intensities of the Bragg peaks as function of *T*.

Fig. S4

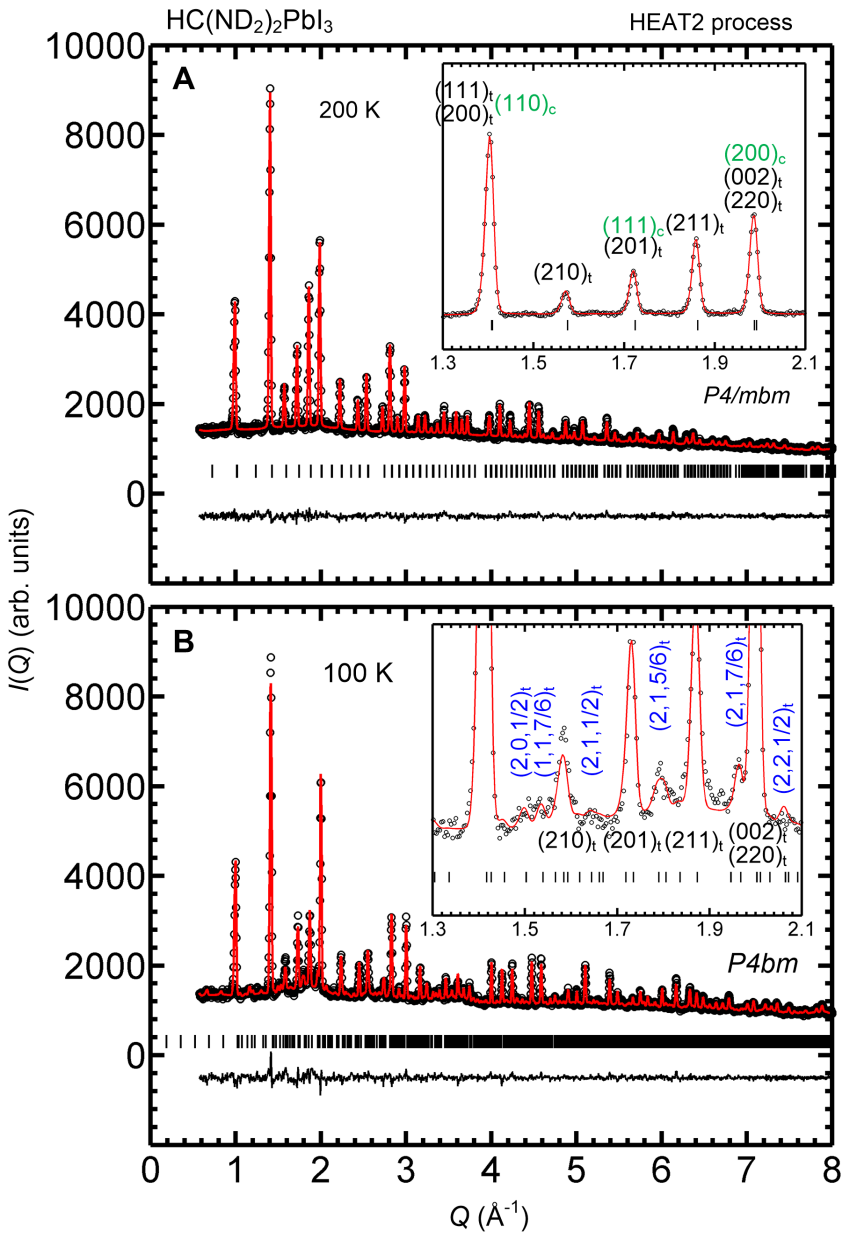

Fig. S4: $HC(ND_2)_2PbI_3$ neutron powder diffraction data. Data are obtained at BT1, NCNR. Neutron diffraction data taken at (*A*) 200 K (Tet IT phase) and (*B*) 100 K (Tet LT phase). The open circles, red lines, black tick marks, and black lines at the bottom are the experimental data, Rietveld refinement results, Bragg peak positions, and difference between the data and refinement, respectively. In the inset of (*A*), the Bragg peak positions expected for the high temperature cubic phase are written in green for comparison. In the inset of (*B*), the blue indices are the superlattice peaks allowed for the Tet LT phase with the characteristic wavevector of $q = (0,0,1/6)$ that are absent in Tet IT phase. The crystal structures of the Tet IT and Tet LT phases were determined by simultaneous refinement of the neutron diffraction data and the x-ray data. Their structural parameters are listed in Table S4 (Tet IT) and S5 (Tet LT).

Fig. S5

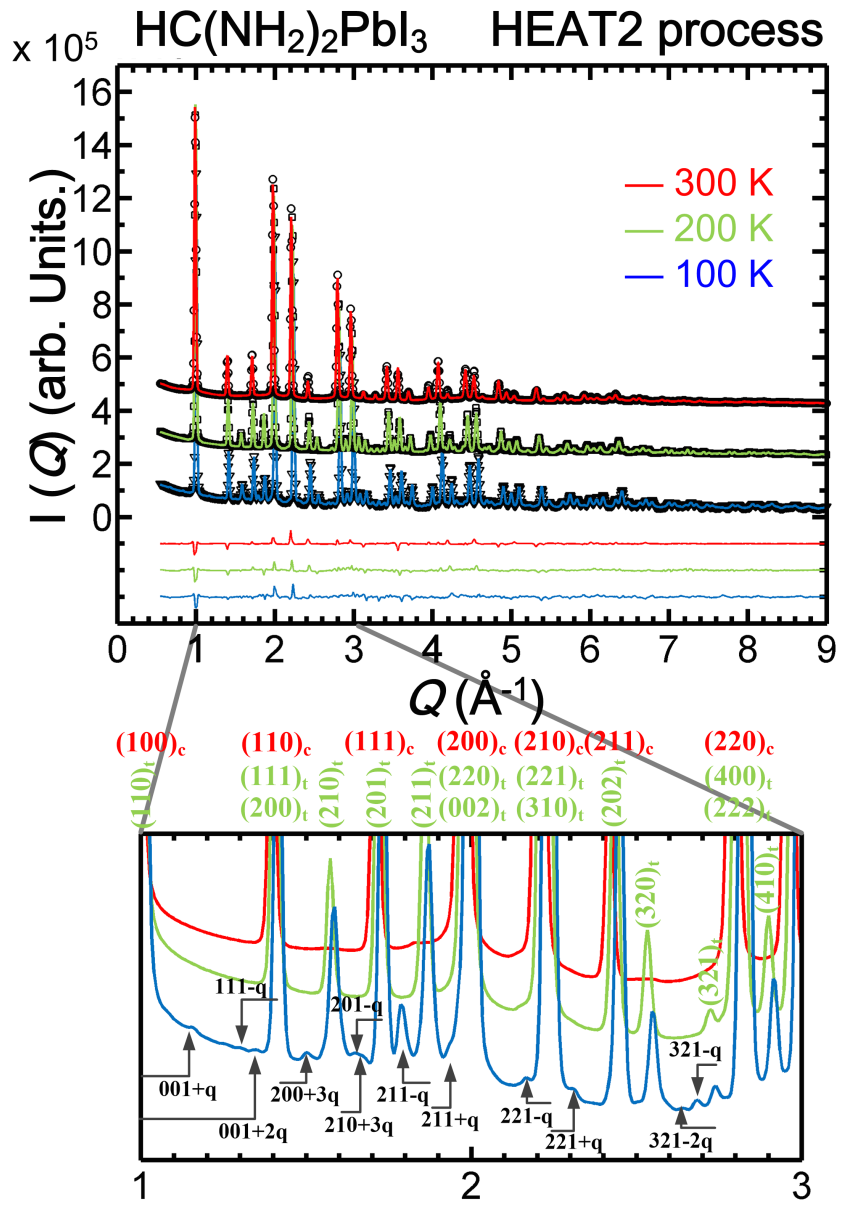

Fig. S5: $HC(NH_2)_2PbI_3$ synchrotron X-ray powder diffraction. Data are obtained at F2, CHESS. The upper panel shows the diffraction patterns obtained at 300 K (cubic phase), 200 K (Tet IT phase) and 100 K (Tet LT phase). The open symbols, thick colored lines over the symbols, and thin black lines at the bottom are the experimental data, Rietveld refinement results, and difference between the data and refinement, respectively. The lower panel shows an enlarged view of the data over a narrower range of Q from 1.0 $Å^{-1}$ to 3.0 $Å^{-1}$. Red and green indices on the top are the Bragg peak positions of the cubic and Tet IT/Tet LT phases, respectively. The panel shows the weak supperlattice peaks with $q = (0,0,1/6)$ that are present in the Tet LT phase. This means that the Tet LT phase adopts a 1×1×6 supercell of the Tet IT phase.

Fig. S6

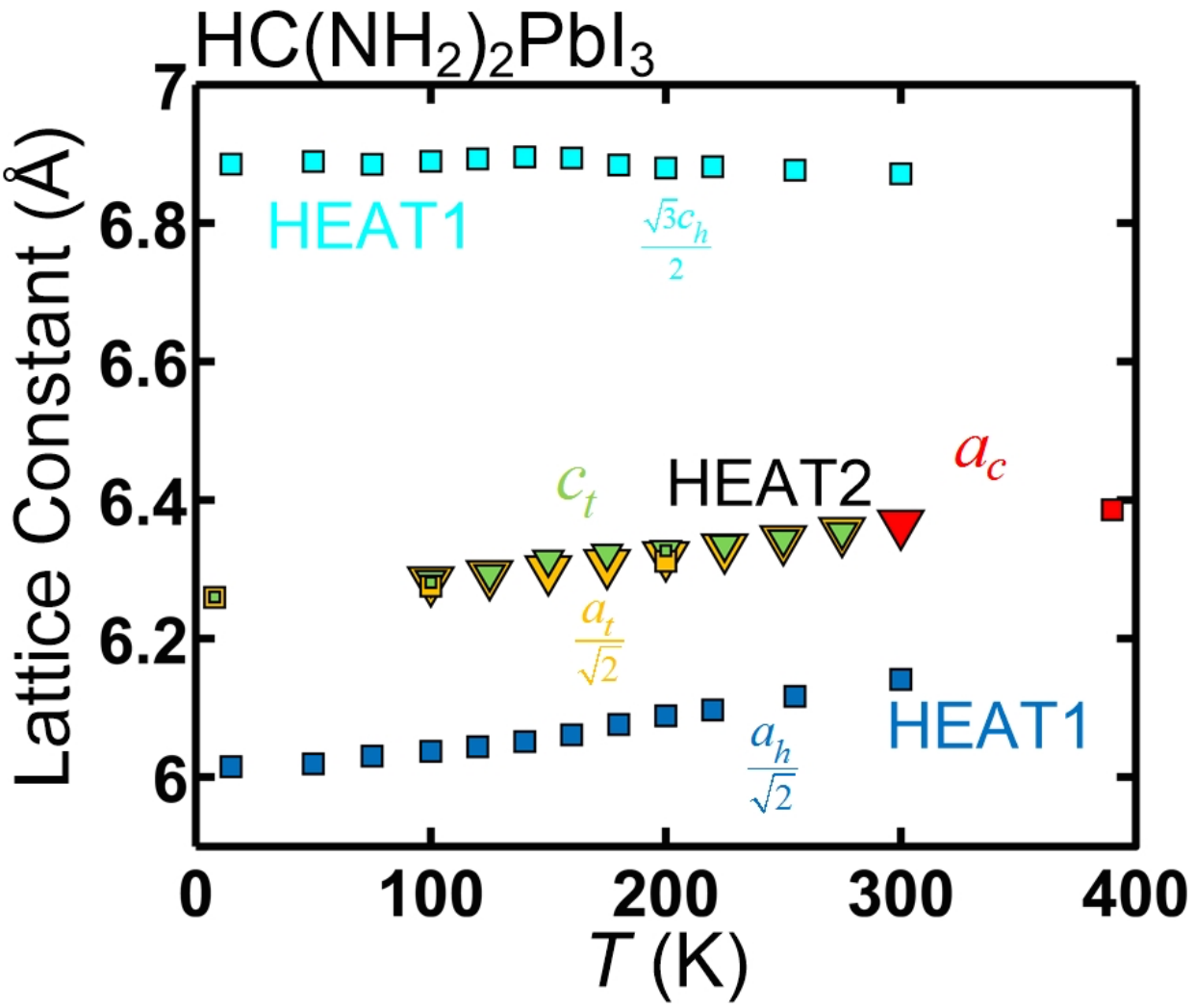

Fig. S6: Lattice constants of $HC(ND_2)_2PbI_3$ as a function of temperature. The lattice constants determined by the Rietveld refinements of neutron diffraction (squares) and synchrotron x-ray (triangles) data, some of which are shown in Fig. S4 and S5, are plotted as a function of temperature; red, orange, and green symbols are a_c, $\frac{a_t}{\sqrt{2}}, c_t$, respectively, where a_c is the cubic lattice constant, and a_t, c_t are the lattice constants of the Tet IT phase. The squares in cyan and blue are the lattice constants for the hexagonal phases, $\frac{a_h}{\sqrt{2}}$ and $\frac{\sqrt{2}c_h}{2}$, some of which have been reported in Ref. (S3).

Fig. S7

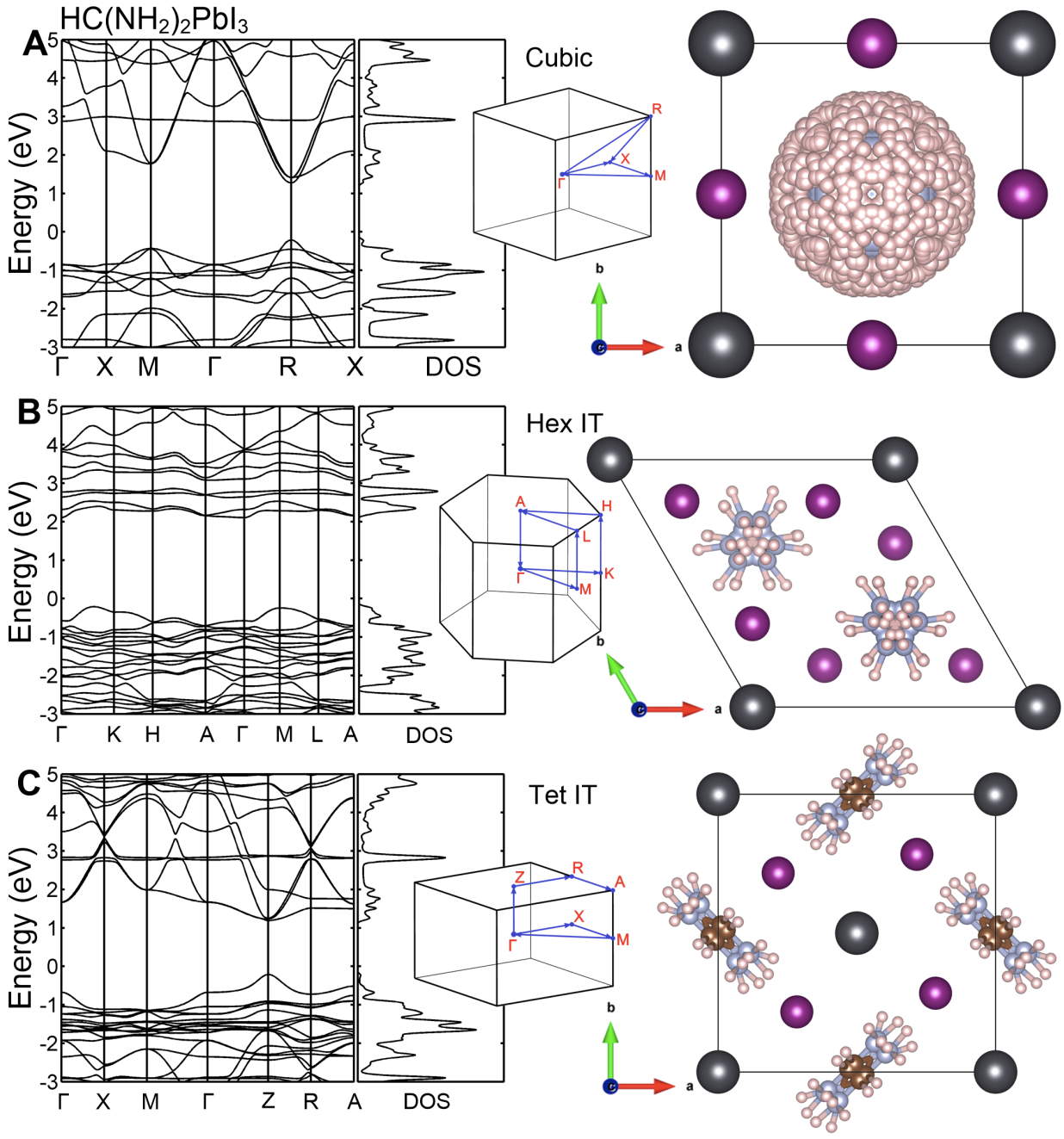

Fig. S7: Electronic band structure of $HC(NH_2)_2PbI_3$ for the cubic, Hex IT and Tet IT phases. Electronic band structures were obtained by DFT calculations for (*A*) the cubic, (*B*) Hex IT and (*C*) Tet IT phases of $HC(NH_2)_2PbI_3$.

Fig. S8

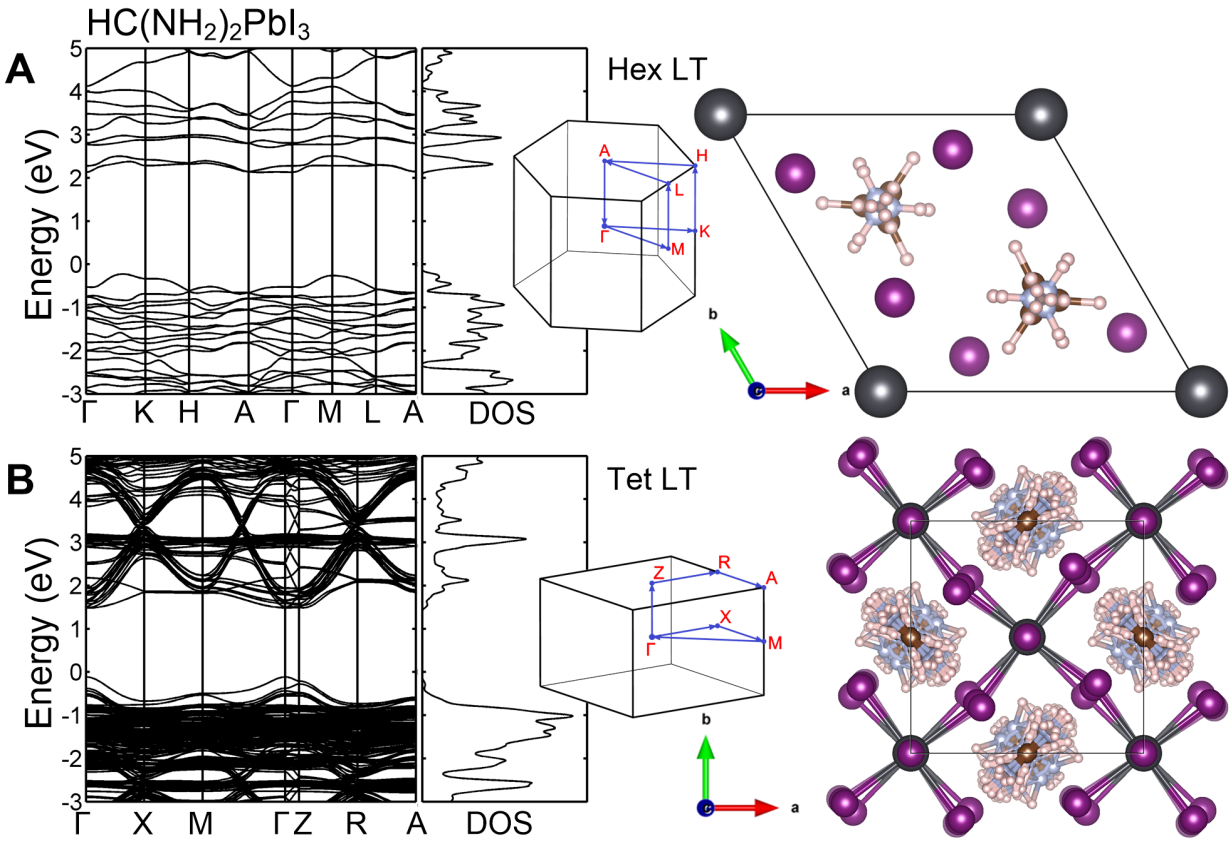

Fig. S8: Electronic band structure of $HC(NH_2)_2PbI_3$ for the Hex LT and Tet LT phases. Electronic band structures were obtained by DFT calculations for (*A*) Hex LT and (*B*) Tet LT phases. The crystal structures for Hex IT phases were taken from Ref. (S3), while the crystal structure of the Tet LT phase was determined by Rietveld refinement of neutron diffraction and synchrotron x-ray data taken at 100 K. Here all the crystallographically equivalent positions of the FA^+ molecule are shown. The geometry of a single FA^+ molecule is shown in the inset of Fig. 5*F*.

Fig. S9

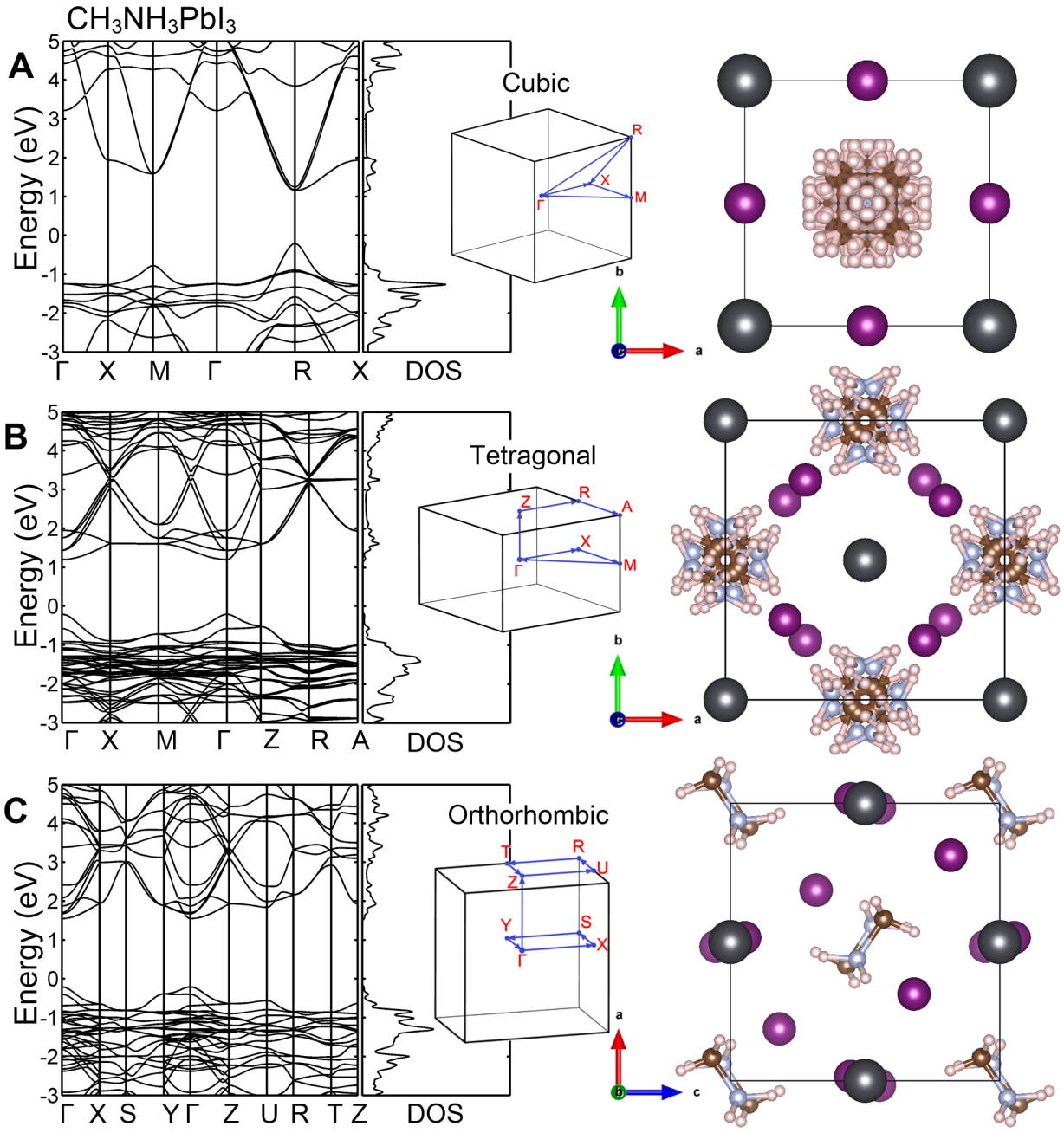

Fig. S9: Electronic band structure of $CH_3NH_3PbI_3$. Electronic band structures were obtained by DFT calculations for (*A*) cubic, (*B*) tetragonal and (*C*) orthorhombic phases of $CH_3NH_3PbI_3$. The crystal structures used were from previous neutron and x-ray diffraction studies (S8, S9).

Fig. S10

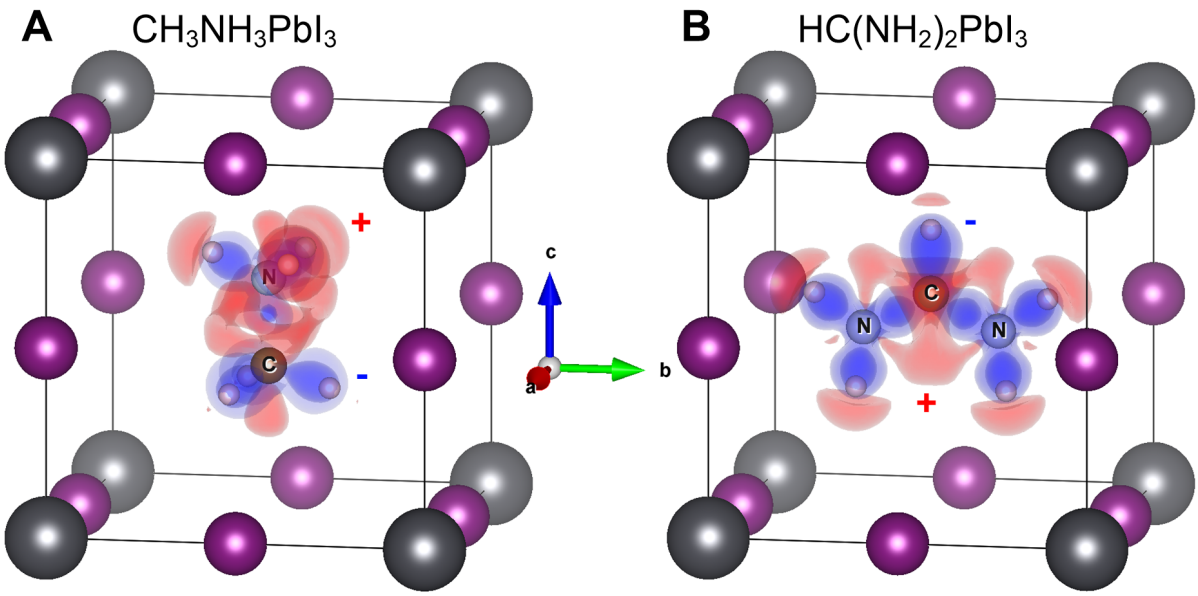

Fig. S10: Electronic charge densities of $CH_3NH_3^+$ and $HC(NH_2)_2^+$ cations. In order to show clearly the electric polarity in the molecule, the charge density was subtracted from a direct sum of single-atom charge densities of each atom. The blue and red surfaces are isosurfaces of "excessive" electrons and holes, respectively.

Fig. S11

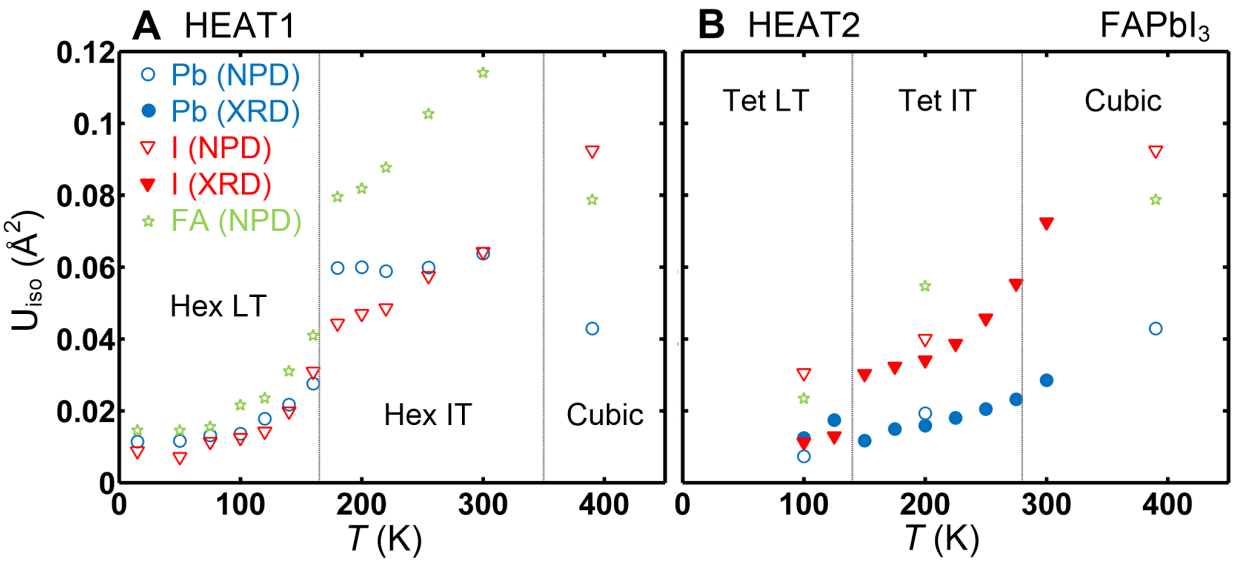

Fig. S11: Isotropic thermal factor of Pb, I and organic cation of $FAPbI_3$ as a function of temperature. These factors were obtained for (*A*) HEAT1 and (*B*) HEAT2 by Rietveld refinement of synchrotron X-ray (filled symbols) and neutron (open symbols) diffraction data.

Fig. S12

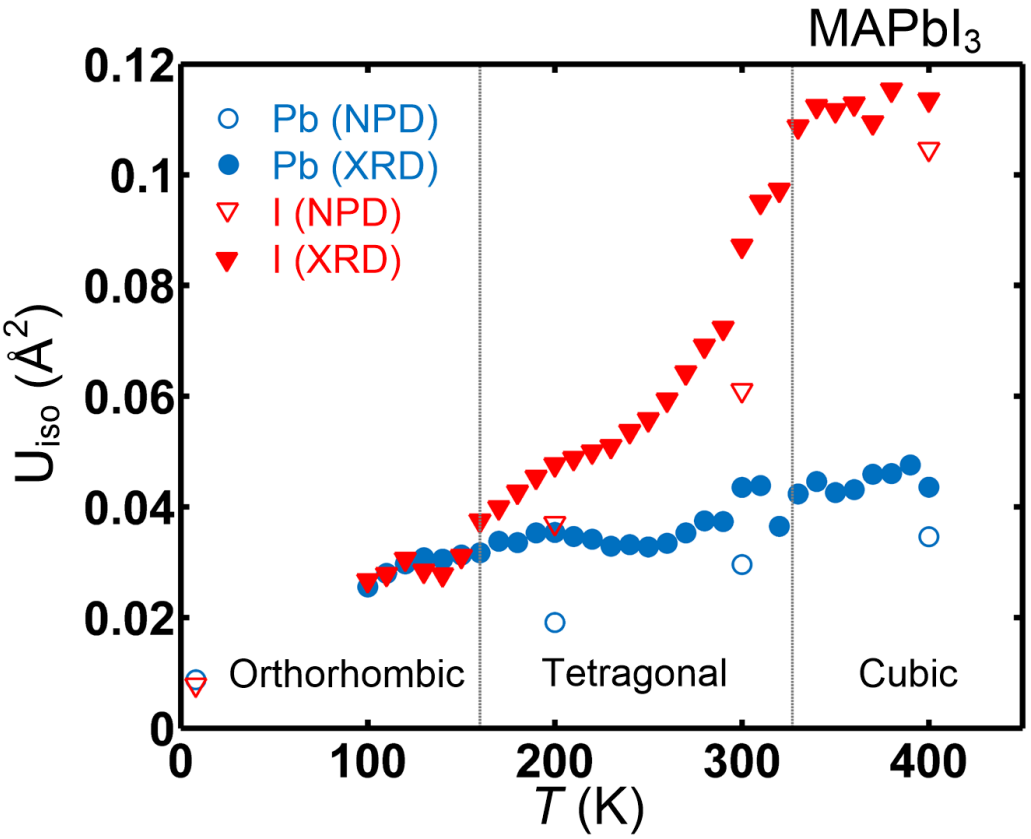

Fig. S12: Isotropic thermal factor of Pb, I and organic cation of $MAPbI_3$ as a function of temperature. These factors were obtained by Rietveld refinement of synchrotron X-ray (filled symbols) and neutron (open symbols) diffraction data.